Advanced Functional Materials

ADVANCED FUNCTIONAL MATERIALS
www.afm-journal.de

RESEARCH ARTICLE OPEN ACCESS

Bio-Inspired Synthesis of Macroporous Single Crystal Particles as Scattering Agents

Stephanie E. Foster[1,2] | Gianni Jacucci[3,4] | Ouassef Nahi[1] | Thomas Kress[3] | Zabeada Aslam[5,2] | Stuart Micklethwaite[5,2] | Alexander N. Kulak[1] | Rik Drummond-Brydson[5,2] | Melinda J. Duer[3] | Yi-Yeoun Kim[1,2] | Silvia Vignolini[3,6] | Fiona C. Meldrum[1,2]

[1]School of Chemistry, University of Leeds, Leeds, UK | [2]The Bragg Centre for Materials Research, University of Leeds, Leeds, UK | [3]Yusuf Hamied Department of Chemistry, University of Cambridge, Cambridge, UK | [4]Department of Physics, University of Calabria, Rende CS, Italy | [5]School of Chemical and Process Engineering, University of Leeds, Leeds, UK | [6]Max Planck Institute for Colloids and Interfaces, Golm(Potsdam), Germany

Correspondence: Stephanie E. Foster (S.E.Foster@leeds.ac.uk) | Silvia Vignolini (sv@mpikg.mpg.de) | Fiona C. Meldrum (F.Meldrum@leeds.ac.uk)

Received: 28 April 2026 | **Revised:** 28 May 2026 | **Accepted:** 5 June 2026

Keywords: calcite | calcium carbonate | porous | structural colour | whitening-agent

ABSTRACT

Introducing controlled porosity into crystalline materials endows them with properties not exhibited by their solid counterparts. However, producing microparticles that combine submicron macroporosity and uniform particle shapes remains a significant challenge. Here, we present a general strategy that yields unique single-crystal microparticles with closed-cell macropores (300–500 nm), a size ideal for generating structural colour. Using a bioinspired approach, we occlude three distinct additives, polystyrene microspheres, polymer vesicles, and amino acids, within 10–20 μm calcite ($CaCO_3$) single crystals. Remarkably, after thermal annealing, all systems are transformed into particles with well-defined shapes and macroporosity, while retaining their single-crystal character. This is particularly surprising for the amino acids, which are originally distributed as individual molecules throughout the crystal lattice. Mechanistic studies using solid state NMR and in situ TEM directly track pore formation and reveal that co-occluded water associated with the amino acids is crucial in creating the pores. This simple method—where the occlusion of amino acids is scalable and compatible with industrial calcite synthesis—delivers a new class of macroporous microparticles suited to coatings, fillers and photonic applications, where their bright white appearance and intense broadband light reflection makes them an environmentally-benign alternative to titanium dioxide for whitening applications.

1 | Introduction

Porous solids represent one of the most important classes of functional materials due to their huge range of potential applications. These include vital processes such as catalysis, filtration, adsorption, separation and thermal insulation [1–3], where the ability to tailor the composition and structure—including the porosity, size distribution, shape and connectivity of the pores—is key to optimising properties and performance. High surface areas and open pore structures are essential for applications such as catalysis that rely on chemical interactions at a surface, while the reduction in density associated with the formation of highly porous materials is beneficial for applications requiring lightweight but mechanically robust materials, such as aircraft components [4]. While exceptional control can be achieved when synthesising micro- and meso-porous materials such as zeolites [5–8], MOFs [9–11] and mesoporous silicas [12, 13], synthesis of macroporous materials with well-defined pores in the submicron range is far more challenging [4, 14, 15]. Approaches including the partial sintering of powders, direct foaming, replica methods, sacrificial pore formers, gel-casting, freeze-casting and additive manufacturing are widely used, but vary significantly

in terms of the porous structure generated and the ability to scale-up the synthesis [4]. As a further consideration, while some of these methods can be used to create macroporous monoliths with the desired morphology [1], it is extremely difficult to generate macroporous particles with well-defined external sizes and shapes.

Here, we present a novel strategy that produces inorganic single crystals with well-defined macroporous structures (pores sizes 300–500 nm) and uniform shapes and sizes (10–20 μm). That these macroporous particles are single crystals and have closed-cell porosity makes them structurally unique, where the air-filled pores are entirely enclosed within the impermeable host crystal. The method builds on an approach inspired by biomineralization: the ability to incorporate additives within single crystals. Biominerals are invariably composite materials, where organic macromolecules are intimately associated with inorganic crystals [16, 17]. While this is readily achieved for polycrystalline materials such as nacre, where organic molecules can be located between the crystal units [18, 19], single crystal biominerals such as the calcite ($CaCO_3$) spines of sea urchins are usually also composites, where protein aggregates are occluded within the crystal lattice, enhancing mechanical properties [20–22]. Despite crystallisation being used as a means of purification, nature therefore demonstrates that it is possible to occlude foreign species within single crystals.

Building on this strategy, it is now established that multiple soluble additives ranging from small molecules [23–26] and proteins [20, 27], to organic [28–30] and inorganic [31–33] nanoparticles and even micron-scale particles [34, 35] can be incorporated within calcite single crystals using a simple one-pot method in which calcium carbonate is precipitated from solution in the presence of the additives. The additives are distributed throughout the crystal matrix, and the level of occlusion depends on the crystal growth rate and the balance between the strength of interaction between the crystal and the additive, where values of 7 mol% have been reported for glycine [23] and ≈70 wt.% for polymer-functionalised gold nanoparticles [36].

This bio-inspired strategy was used here to generate porous crystals, where we hypothesised that thermal annealing of composite crystals containing spherical organic particles would burn off the organic material, generating porosity. Three very different types of additives—solid polystyrene (PS) microspheres, water-filled polymeric vesicles and small amino acid molecules—are occluded within calcite single crystals, and these composite crystals are thermally annealed to generate porosity, where the single crystallinity of the host crystal is preserved after annealing (Figure 1). We demonstrate that each additive leads to a structurally unique crystal whose porosity can be further tuned by varying the annealing conditions. That macroporous crystals can be generated from composite crystals containing small molecules (here amino acids) is particularly surprising, and the mechanism of pore formation is characterised using in situ transmission electron microscopy (TEM) and solid-state NMR.

We then explore a potential technological application of these particles, where their micron-scale dimensions, pore sizes of hundreds of nanometres and closed-cell porosity make them ideal scattering agents whose properties are retained on immersion in different media. While titania has been the traditional material of choice of whitening agent [37] due to its high refractive index [38], economic, regulatory, health and sustainability concerns are now driving a global effort to identify alternatives [39–44]. Notably, our macroporous crystals reflect strongly across the visible spectrum, achieving up to 70% efficiency with particles just 11 μm in thickness. Introduction of porosity into calcium carbonate therefore transforms the crystals into effective, environmentally-friendly whitening agents that offer a real alternative to titania (TiO_2). With the recognised ability to incorporate additives into a wide range of crystalline materials, this novel experimental strategy represents a flexible, inexpensive and scalable approach for generating macroporous particles with uniform sizes and tunable porosities in the difficult-to-access sub-micron range, and potentially creating materials that can address complex performance standards.

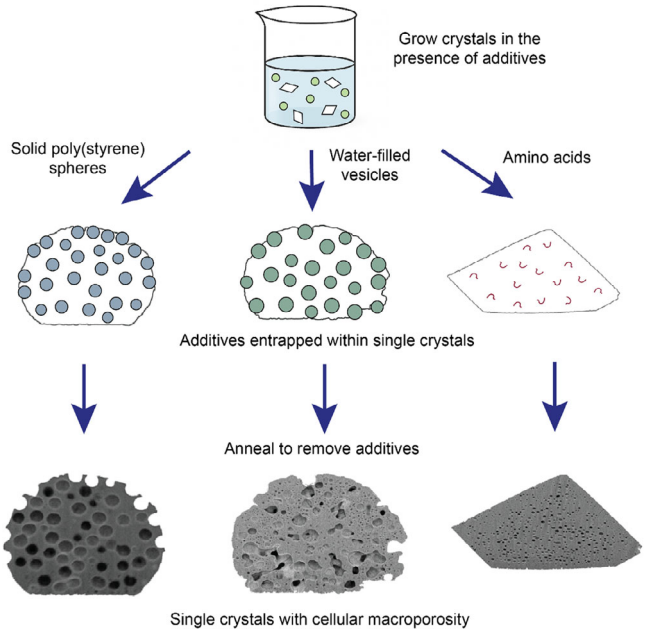

FIGURE 1 | Schematic diagram of the strategy used to generate macroporous single crystals.

2 | Results and Discussion

2.1 | General Strategy

Solid PS microspheres were selected as initial candidates, where these were anticipated to generate voids of comparable size and shape to the original particles. The optimal size and incorporation level of particles for our target application of whitening agents was estimated using reflectance simulations (see SI for details). Spherical voids were employed in the models, and optimal scattering was achieved for voids of 500 nm and a volume fraction of ≈0.4 (Figure S1). 500 nm PS spheres were therefore used in the experiments and the relationship between the additive type, annealing conditions (heating rate, temperature, duration) and porosity was investigated to optimise structure/ property relationships and create highly reflective crystals that appear white.

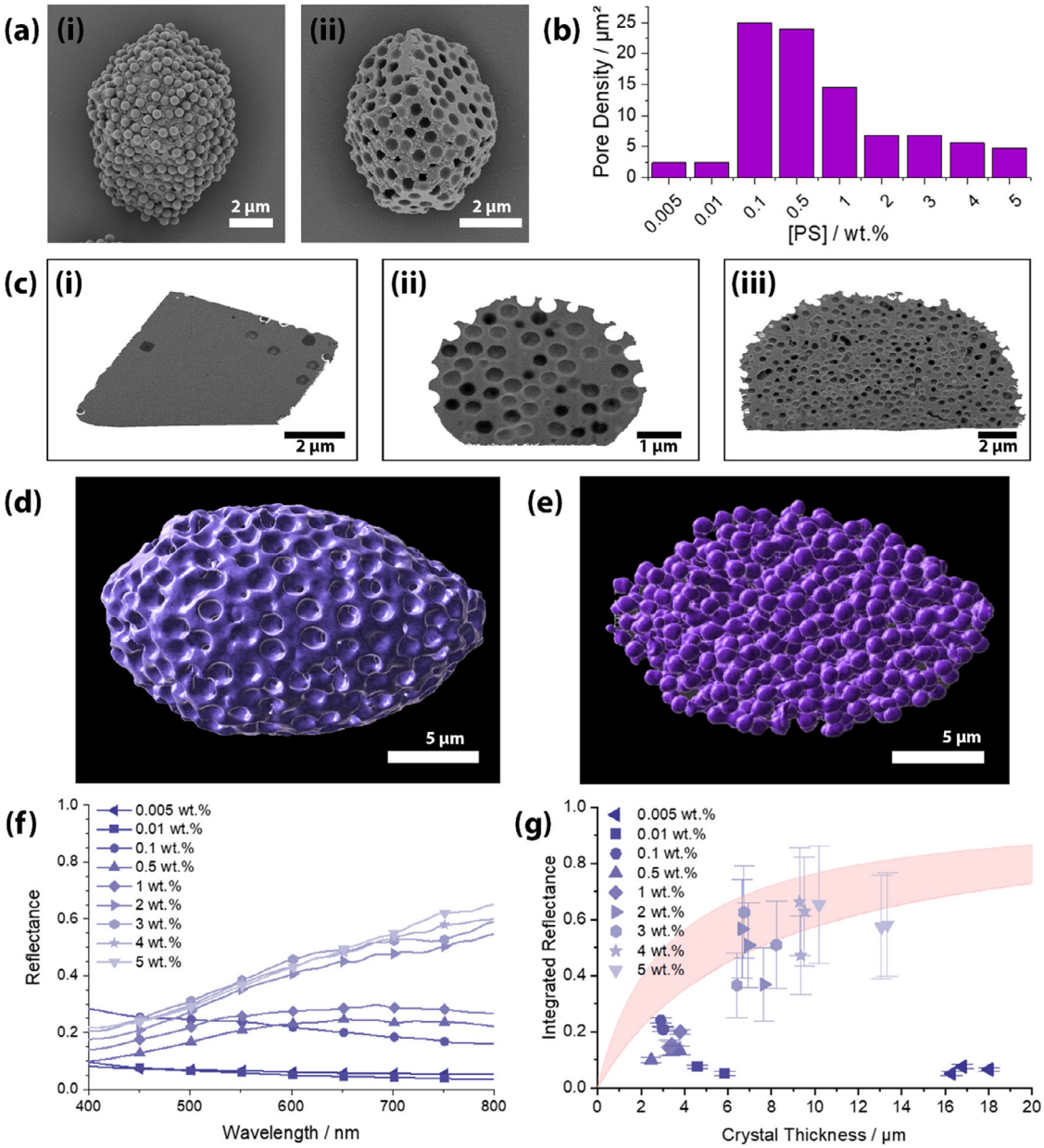

FIGURE 2 | Porosity and optical properties of Calcite-PS crystals. (a) Calcite-PS crystal prepared at $[Ca^{2+}] = 1.25$ mM and [PS] = 2 wt.% (i) before and (ii) after annealing. (b) Areal pore density of annealed calcite-PS prepared using different [PS]. (c) FIB-SEM cross-section images of annealed calcite-PS crystals prepared with [PS] (i) 0.01 wt.%, (ii) 1 wt.% and (iii) 4 wt.% (see full range of Calcite-PS FIBSEM images in SI). (c) Pore density of annealed calcite-PS crystals prepared using different [PS]. (d,e) Reconstructed 3D FIB-SEM tomograms of annealed calcite-PS crystals prepared at (d) $[Ca^{2+}] =$ 1.25 mM and [PS] = 1 wt.%, where (d) shows the external crystal and (e) shows the internal porosity (see Movie S1 for the full FIB-SEM tomogram). (f) Reflectance spectra of annealed calcite-PS crystals prepared at different [PS] and (g) integrated reflectance as a function of crystal thickness compared with the simulated industry standard (shaded region).

2.2 | Creating Porosity With Polystyrene (PS) Microspheres

Calcite crystals containing PS microspheres (Calcite-PS crystals) were synthesised by precipitating calcium carbonate from calcium chloride solution in the presence of 500 nm high acid content carboxylate-functionalised PS particles, using the ammonia-diffusion method [45]. The surface charge density and chemistry of these functionalised particles facilitates effective binding to the calcite surface and incorporation within the crystals (Figure 2a) [34]. A range of PS concentrations ([PS]) were tested to create composite crystals with varying levels of incorporation and samples were then annealed using a standard protocol (heat at a rate of 5°C min^{-1} and hold at 500°C for 30 min). This causes the PS spheres to decompose, leaving highly uniform 500 nm spherical voids in place of the occluded PS spheres (Figure 2a,b).

The porosity of the product crystals was characterised using focused ion beam scanning electron microscopy (FIB-SEM)

tomography, and by analysing cross-sections of the crystals prepared using FIB-SEM, such that datasets were typically derived from measurement of 100s to1000s of pores. The tomograms demonstrated that the porosity is closed-cell such that the crystals can be immersed in any medium while maintaining the air-filled pores. The porosity was quantified by determining the areal pore density (the number of pores present per μm2) and the pore area fraction (the percentage of the crystal cross-sectional area occupied by pores).

Annealed calcite-PS crystals grown at $[Ca^{2+}] = 1.25$ mM were analysed to determine the effect of the [PS] on porosity (Figure 2b,c; Figure S3). Crystals grown using [PS] = 0.005 and 0.01 wt.% exhibited low incorporation and porosity, with very few pores present within the crystal. A uniform distribution of the pores throughout the crystals was achieved at [PS] = 0.1 wt.% and above, and a maximal pore density of 25 μm^{-2} at [PS] = 0.1 wt.%. Little change occurred on increasing the [PS] to 0.5 wt.%, but the pore density dropped upon further increase of [PS] and ultimately reached 5 μm^{-2} at [PS] = 5 wt.%. This reduction in pore density can be attributed to greater PS occlusion with increasing [PS]. As a greater number of PS spheres are occluded, the proximity between nearest neighbours decreases and occluded PS spheres are more likely to touch. This results in a higher incidence of large pores or channels after heating and reduces the overall pore density. Measurement of the area occupied by the pores yielded a maximum value of 36% for samples prepared with 2 wt.% PS spheres. Confirmation of uniform porosity in 3 dimensions was achieved by constructing tomograms based on images of consecutive FIB-SEM slices (Figure 2d,e; Movie S1).

The optical properties of the annealed calcite-PS crystals were assessed using micro-spectroscopy to determine the reflectance as a function of the wavelength of the incident light (Figure 2f). Because the measured reflectance is also dependent on crystal size, the thickness of each particle was measured using SEM to evaluate how reflectance varies with thickness across the full wavelength range. Unannealed calcite-PS composites and annealed calcite crystals were both poorly reflective (Figures S4 and S5), demonstrating that simple occlusion of the PS spheres had a minimal effect on crystal reflectance. In contrast, annealed calcite-PS crystals exhibited a boost in reflectance due to the greater difference in refractive index between the crystal and air-filled pore than between the crystal and PS sphere.

As expected, the reflectance of these crystals depends on their porosity, with higher pore densities yielding higher reflectance. Annealed calcite-PS with very low pore densities (prepared at [PS] = 0.005 and 0.01 wt.%) had poor reflectance comparable to the annealed calcite crystals, while those with a uniform distribution of pores ([PS] = 0.1–1 wt.%) had significantly greater reflectance (a factor of 3–4 times at $\lambda = 800$ nm). This increased further to ≈10 times for [PS] = 2–5 wt.%. However, higher [PS] was associated with a loss of broadband reflectance, with the reflectance of crystals grown at [PS] = 2–5 wt.% dropping in the blue wavelength region due to the absorption of light by PS residues. This was attributed to residual polymers, which was also apparent from the yellow colour of annealed calcite-PS crystals with higher [PS] (Figure S6).

Finally, the reflectance of the crystals was evaluated as a function of their thickness, and an analytical theory (Figure S2) was used to compare them with the whitening agents used in industry (Figure 2g). Importantly, the porous calcite microparticles are finite heterogeneous scattering media rather than homogeneous pigment particles. Each microparticle consists of a continuous calcite matrix containing air-filled inclusions. These pores act as internal scattering centres, analogous to scattering particles in a conventional white film, while the crystal thickness defines the optical path length through the scattering medium.

The performance of a material as a whitening agent is traditionally evaluated by estimating its scattering mean free path, an intrinsic material property independent of thickness. Values of 1–2 μm are optimal for industrial applications as they align with the performance range of state-of-the-art TiO_2 pigments [38] and emerging bioinspired alternatives, and were used in the calculations [46–49]. This is shown as a shaded area in the graph shown in Figure 2g and their performances are referred to as the "industry standard". This comparison benchmarks the intrinsic scattering efficiency of the porous crystal architecture, rather than constituting a direct measurement of a formulated coating. Notably, several annealed calcite-PS crystals prepared at [PS] = 2–5 wt.% had values that are equivalent to, or even superior to the simulated materials, demonstrating that our synthesis strategy delivers calcium carbonate particles that are effective whitening agents.

2.3 | Creating Porosity Using Vesicles

An alternative additive system was therefore explored to reduce residual organics and eliminate unwanted absorbance. Calcite crystals were precipitated in the presence of poly(methyacrylic acid)-poly(benzyl methacrylate) (PMAA-PBzMA) vesicles of diameter 365 ± 120 nm by direct mixing of the calcium solution with sodium carbonate solution, where these polymer vesicles are decorated with carboxylate-functionalised chains that facilitate effective occlusion. As for calcite-PS, a range of vesicle concentrations ([Ves]) were tested and porous crystals were created by annealing the resulting calcite-Ves composite crystals using the standard protocol.

Cross-sections of annealed calcite-Ves crystals showed that the vesicles were uniformly occluded throughout the crystals and that they were removed by annealing to leave pores (Figure 3a). Unlike the annealed calcite-PS crystals, the pores were seldom spherical, which can be attributed to the significant water content of the vesicles, which facilitates restructuring of the surrounding calcite during annealing. Analysis of the FIB-SEM images showed that pore density increased with [Ves] and reached a maximal value of 27 μm^{-2} at [Ves] = 0.25 wt.% (Figure 3b), comparable to the maximum pore density achieved in annealed calcite-PS crystals (25 μm^{-2}). A maximum area occupied by the pores of 27% was recorded.

All annealed calcite-Ves crystals were more reflective than annealed pure calcite, where crystals formed at [Ves] = 0.05 wt.% reflected around 60% of the incident light (Figure 3c). Little

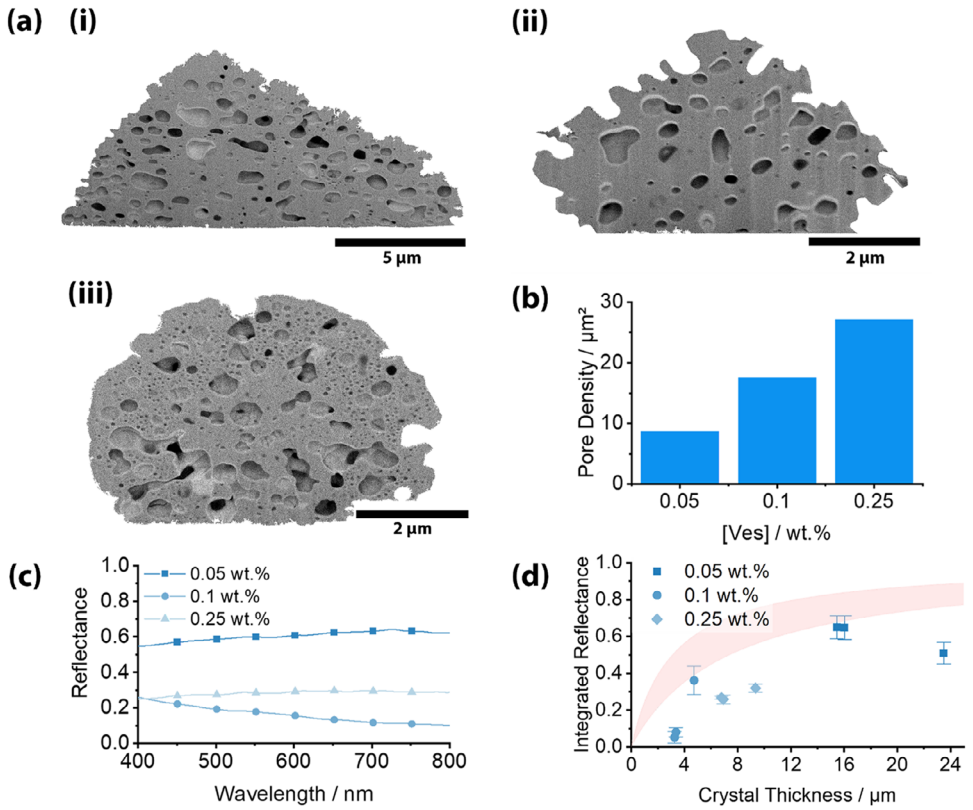

FIGURE 3 | Porosity and optical properties of annealed Calcite-Ves crystals. (a) FIB-SEM cross-section images of a Calcite-Ves crystal prepared with [Ves] = (i) 0.05 wt.%, (ii) 0.1 wt.% and (iii) 0.25 wt.%. (b) Areal pore density and (c) reflectance spectra of annealed Calcite-Ves crystals prepared using different [Ves]. (d) Integrated reflectance as a function of crystal thickness and compared with the simulated industry standard (shaded region).

absorbance occurred in the blue region, confirming the complete removal of the polymer. Annealed calcite-Ves crystals grown at [Ves] = 0.1 wt.% exhibited a gradient in the reflectance with a minimum in the red region, where absorbance in this region produces a blue colour that enhances the perception of bright white [50]. Consideration of the integrated reflectance as a function of thickness showed that a number of annealed calcite-Ves crystals prepared at [Ves] = 0.05 and 0.1 wt.% were very close to the simulated industry standard (Figure 3d). With lower initial polymer content than the calcite-PS samples and superior broadband reflection, the annealed calcite-Ves crystals are competitive with those generated by PS occlusion.

2.4 | Creating Porosity Using Amino Acids

2.4.1 | Generating Porous Crystals

As our third category of porogen, we investigated the possibility of creating porous calcite crystals by annealing crystals containing amino acids [23, 51], where this process is cost-effective and scalable. As a precedent, calcite sea urchin spines have been shown to become porous on heating [22, 52]. However, it is noted that these biominerals are quite different in structure from synthetic calcite/ amino acids crystals, where they contain aggregates of protein molecules [53, 54] and amorphous calcium carbonate (ACC). In contrast, the synthetic crystals do not contain ACC and the amino acids are distributed as individual molecules throughout the crystal lattice [23].

Crystals were grown at $[Ca^{2+}]$ = 1.25–10 mM and [amino acids] = 10–50 mM, and incorporated up to 1.2 mol% Asp and 1.9 mol% Gly (Figure S7). Cross-sectional FIB-SEM images showed that all annealed crystals were highly porous. There was a broad range of pore sizes and shapes, and some pores were faceted (Figures 4a and 5a; Figures S8 and S9). Annealed calcite-Asp crystals grown at $[Ca^{2+}]$ = 1.25 mM possessed low pore densities (2–4 μm^{-2}) (Figure 4a,b), while samples prepared at $[Ca^{2+}]$ = 5 mM and [Asp] = 50 mM had values of 13 μm^{-2}. Further increase of $[Ca^{2+}]$ to 10 mM then reduced the pore density. This is attributed to greater incorporation of Asp, which creates a higher number of pores during the initial annealing, but their close proximity causes them to coalesce as heating continues.

FIB-SEM tomograms of the annealed calcite-Asp crystals prepared at $[Ca^{2+}]$ = 10 mM, [Asp] = 10 mM again confirmed uniform porosity (Figure 4b,c; Movie S2). For the annealed calcite-Gly crystals, the pore density generally increased with both $[Ca^{2+}]$ and [Gly] in the regimes $[Ca^{2+}]$ = 1.25–10 mM and [Gly] = 100–200 mM (Figure 5b). One exception was crystals formed with $[Ca^{2+}]$ = 10 mM and [Gly] = 200 mM, which had lower pore densities than those formed at $[Ca^{2+}]$ = 10 mM and [Gly] = 100 mM. The maximum area occupied by the pores for calcite-Asp and calcite-Gly samples prepared using the standard heating protocol was

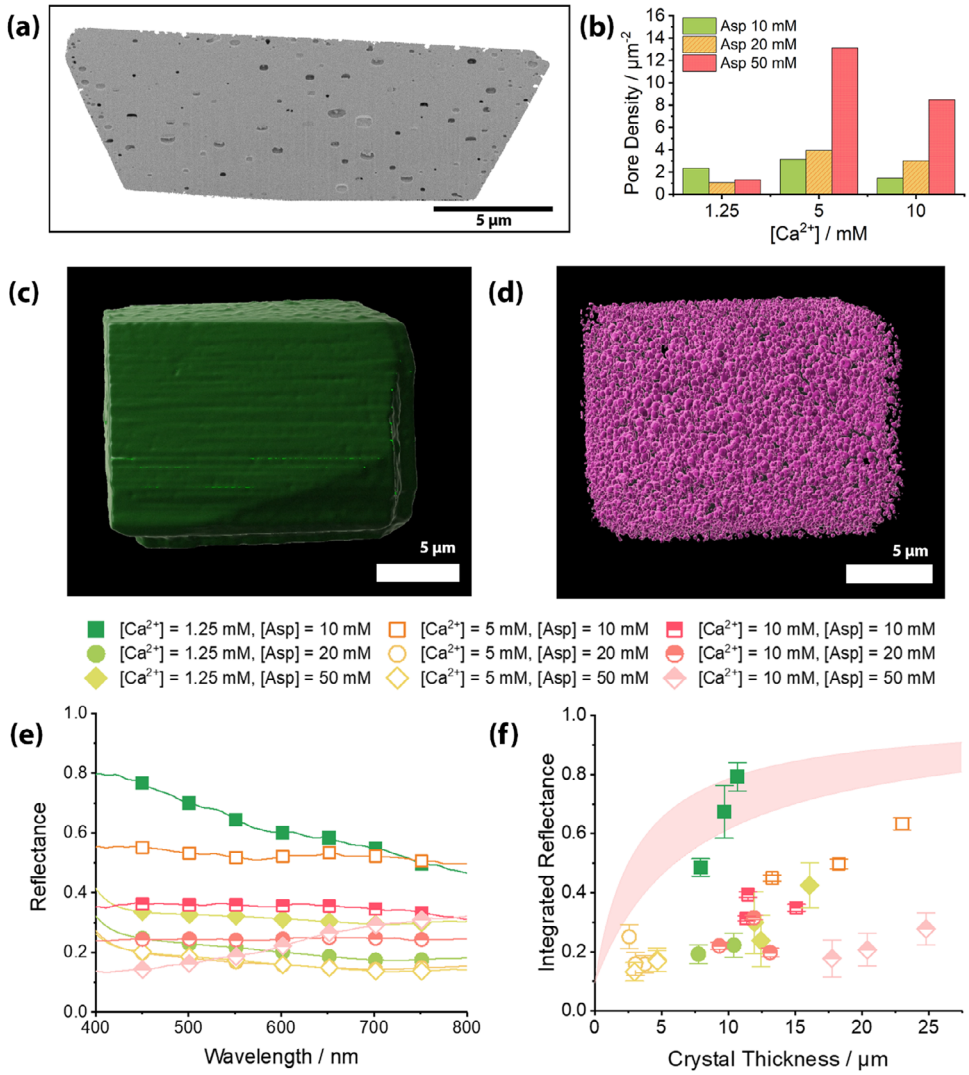

FIGURE 4 | Porosity and optical properties of annealed Calcite-Asp crystals. (a) FIB-SEM cross-section of a calcite-Asp crystal prepared with [Ca^{2+}] = 1.25 mM and [Asp] = 10 mM. (b) Variation of pore density with [Asp] and [Ca^{2+}]. (c,d) Reconstructed 3D FIB-SEM tomograms of annealed calcite-Asp crystals prepared at [Ca^{2+}] = 10 mM and [Asp] = 10 mM), where (c) shows the external crystal and (d) shows the internal porosity (see Movie S2 for the full FIB-SEM tomogram). (e) Reflectance spectra of annealed calcite-Asp crystals prepared at different [Ca^{2+}] and [Asp] and (f) integrated reflectance as a function of crystal thickness and compared with the simulated industry standard (shaded region).

20% for samples prepared at [Ca^{2+}] = 5 mM and [Asp] = 20 mM and 13% for those prepared at [Ca^{2+}] = 10 mM and [Gly] = 100 mM.

2.4.2 | Influence of Annealing Conditions

Insight into the ability to control the porosity and thus the optical properties of the crystals by varying the annealing conditions was gained by studying calcite-Asp crystals formed at [Ca^{2+}] = 10 mM and [Asp] = 10 mM. The influence of the annealing temperature was explored by heating samples to target temperatures of 300°C–600°C at 5°C min^{-1} and annealing for 30 min. The upper limit of 600°C was selected to avoid decomposition of calcite into calcium oxide, which occurs at temperatures >600°C, as confirmed by thermogravimetric analysis (TGA) (Figure S10). The pore densities increased substantially between 300°C (0.5 µm^{-2}) and 400°C (1.3 µm^{-2}) and uniform porosity of ≈1.5 µm^{-2} was achieved after annealing at 500°C. Pore areas increased from 1% to 5% to 12% at 300°C, 400°C and 500°C respectively, showing that pore formation primarily occurs by 400°C (Figure 6a,b).

The annealing times and heating rates also affected the porosity, where the pore density decreased from 1.6 to 1.2 µm^{-2} and the pore area fraction increased from 14% to 22% on extending the annealing time from 30 min to 8 h at 500°C (Figure 6c; Figure S11). This is consistent with a combination of pore growth and coalescence occurring at 500°C. An increase in the heating rate from 1°C to 10°C min^{-1} to a target temperature of 500°C resulted in an increase in the pore density from 1.2 to 2.2 µm^{-2}, with little change in the pore area (Figure 6d). With new pores primarily occurring by 400°C, this behaviour is consistent with the formation of a similar number of pores across all heating rates. However, the longer annealing times experienced by crystals annealed at lower rates enables existing pores to coalesce, reducing the pore density but maintaining a constant pore area.

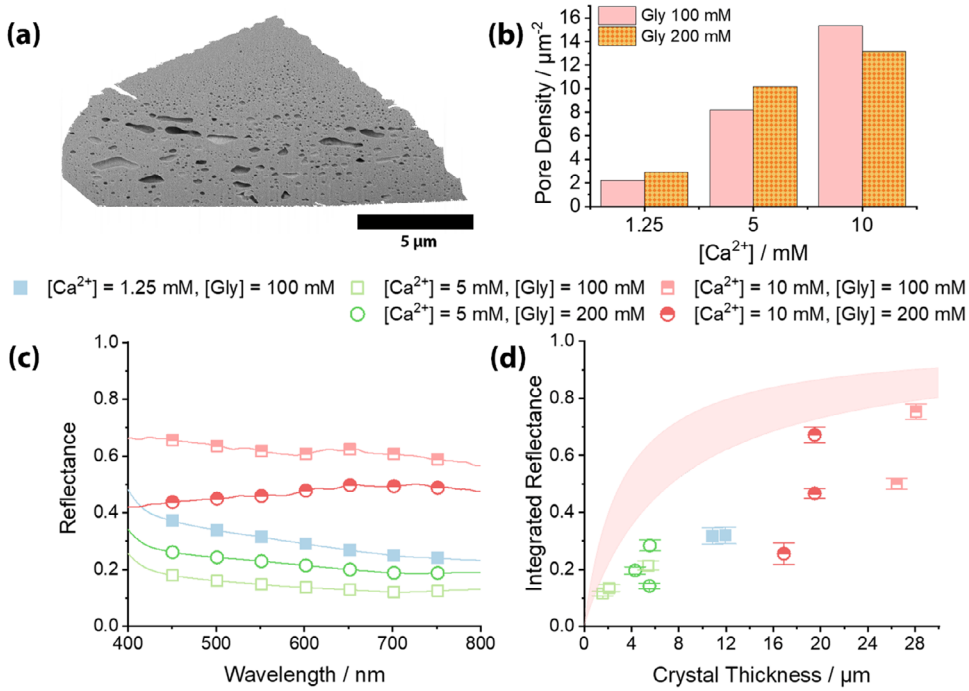

FIGURE 5 | Porosity and optical properties of annealed Calcite-Gly crystals. (a) FIB-SEM cross-sections of a calcite-Gly crystal prepared at [Gly] = 100 mM and $[Ca^{2+}]$ = 10 mM. (b) Variation of areal pore density with [Gly] and $[Ca^{2+}]$. (c) Reflectance spectra of annealed calcite-Gly crystals prepared at different $[Ca^{2+}]$ and [Gly] and (d) integrated reflectance as a function of crystal thickness and compared with the simulated industry standard (shaded region).

2.4.3 | Optical Properties

All of the calcite-Asp (Figure 4e) and calcite-Gly (Figure 5c) crystals annealed under standard conditions exhibited superior reflectance to annealed pure calcite and the vast majority displayed excellent broadband reflectance. Analysis of the optical performance of annealed calcite-Asp crystals as a function of thickness showed that many exceeded the simulated industry standard (Figure 4f). After taking the crystal thickness into account, the annealed calcite-Gly crystals performed somewhat less well than the annealed calcite-Asp crystals. However, some crystals prepared at [Gly] = 200 mM fell just below the simulated industry standard, suggesting that the performance could be further optimised by varying the crystallisation and annealing conditions (Figure 5d).

2.5 | Mechanism of Pore Formation

That removal of the additives occluded within the individual crystals is achieved while retaining their single crystal character is surprising, where cracking could be expected as water and organic residues are released during annealing. The mechanism underlying pore formation was therefore investigated in detail, focusing on calcite-Asp crystals.

Transmission electron microscopy (TEM) was used to study pore formation in situ, where an 80 nm thick lamella of a calcite-Asp crystal grown at $[Ca^{2+}]$ = 10 mM and [Asp] = 10 mM was prepared by FIB lift-out and was imaged while heating at 5°C min^{-1} (Figure S12; Movie S3). 3–5 nm spherical pores were observed to form between 150°C–200°C and are visible as lighter regions in the bright field TEM images. These did not move or visibly grow when heating was continued to 500°C (Figure S13). Markedly different behaviour was observed in thicker (≈200 nm) regions of the lamella lying close to its perimeter. This area contained pores that were ≈25 nm in diameter and delineated by clear facets, giving the square-like cross-sections seen in the FIB-SEM images.

The formation of these geometric pores was further explored by heating a stepped lamella with larger thicknesses ranging from 750–990 nm (Figure 7; Figure S14). The onset of pore formation occurred at a higher temperature than in the 80 nm lamella, where 5 nm spherical pores became visible at 300°C (Movie S4). A range of behaviours were observed, where the pores in the stepped lamella were observed to (i) migrate through the lattice and coalesce during heating, before ultimately reaching fixed positions at 400°C, and (ii) growing without coalescence.

As aspartic acid and glycine decompose at ≈250°C under inert atmospheres [55], the formation of pores at 150°C cannot be due to the degradation of the organic molecules and is attributed instead to water molecules that are occluded together with the amino acids (ie. the individual amino acid molecules do not fully dehydrate during occlusion). This was confirmed using ^{1}H solid state NMR (SS-NMR), where crystals precipitated at $[Ca^{2+}]$ = 10 mM and [Asp] = 50 mM or [Gly] = 400 mM were analysed after heating to 100°C to remove water molecules bound to the surfaces of the crystals (Figure S15). Broad peaks are observed at about 5.2 ppm for both samples after heating to 100°C, which arise from low-mobility water molecules. This is consistent with water entrapped within the crystal lattice. The asymmetric shape of this peak for the calcite-Gly sample is attributed to some residual

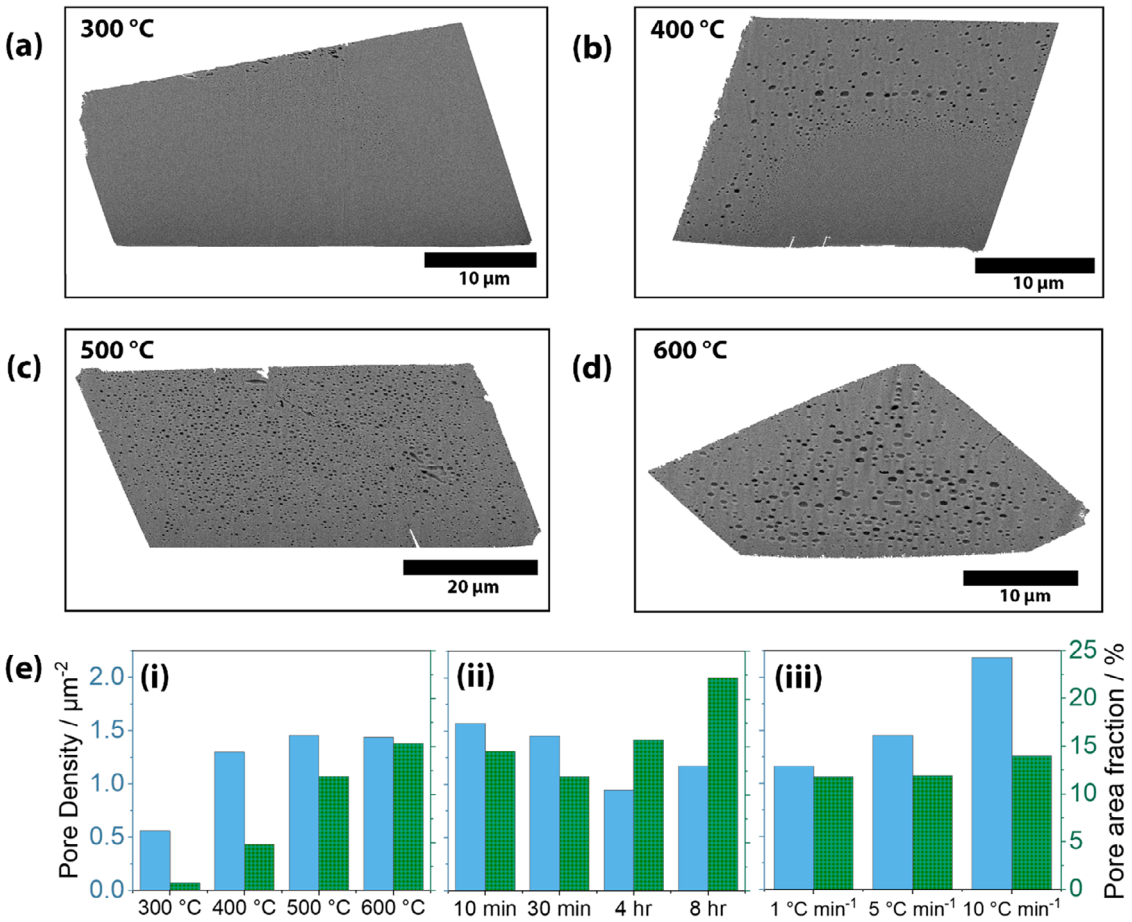

FIGURE 6 | Influence of heating parameters on the porosity of Calcite-Asp crystals prepared at [Asp] = 10 mM and [Ca^{2+}] = 10 mM. (a–d) FIB-SEM cross-sections of Calcite-Asp crystals heated at 5°C min^{-1} and held at the indicated target temperatures for 30 min. (e) Corresponding pore properties of Calcite-Asp crystals, showing the effect of (i) annealing temperature, (ii) annealing time, and (iii) annealing rate. The blue bars show the areal pore density in μm^{-2} (number of pores per μm^2 of crystal) and the green bars show the pore area fraction in % (percentage of the crystal cross section area occupied by pores).

surface-bound water on the crystals, which gives rise to a sharper peak at a lower chemical shift.

More extensive pore formation then occurs above ≈230°C, when the occluded amino acids degrade and release further water molecules [55]. SS-NMR was again used to monitor the changes in the water environment when the crystals were heated to 300°C and 500°C. The band corresponding to the entrapped water molecules becomes sharper and shifts to a higher chemical shift after heating the crystals to 300°C. This indicates that the water molecule are more mobile, which is consistent with them residing within pores rather than the crystal lattice. All water is lost after heating to 500°C, and the SS-NMR spectrum shows only peaks arising from the decomposition of the amino acids.

3 | Discussion

Calcium carbonate is used in enormous quantities in industrial applications such as fillers and coatings due to its low toxicity and cost, its abundance, and ease of synthesis [56]. Control over particle size and shape is essential to many of these applications [57]. For example, smaller, more uniform particles enhance light scattering and thus improve the brightness and opacity of paper and paints, while specific shapes can enhance gloss, uniformity, and processability, making it necessary to precipitate crystals de novo rather than using ground calcium carbonate for many applications [56, 58, 59]. Calcium carbonate is also often selected for its white appearance, where the average refractive index of $n_{590\ nm}$ = 1.658 [60], is larger than most polymers. However, this value is still considerably lower than that of titania (anatase n = 2.55 [61], rutile n = 2.7 [62]). Therefore, if calcium carbonate crystals or comparable minerals are to be considered as alternatives to titania, their size, shape, and internal structure must be controlled to enhance their ability to exhibit effective, broadband scattering. Although it is straightforward to achieve multiple scattering in particles larger than a few millimetres, it is typically highly challenging in particles tens of microns or less in size—the length scale most relevant to coatings and fillers [63].

The methodology presented here generates macroporous inorganic particles with unique structures, where they are single crystals with uniform sizes (10–20 µm) and well-defined external shapes. The macroporosity falls in the difficult–to–access submicron regime, and as single crystals with closed-cell porosity, they are completely impermeable and can be immersed in any

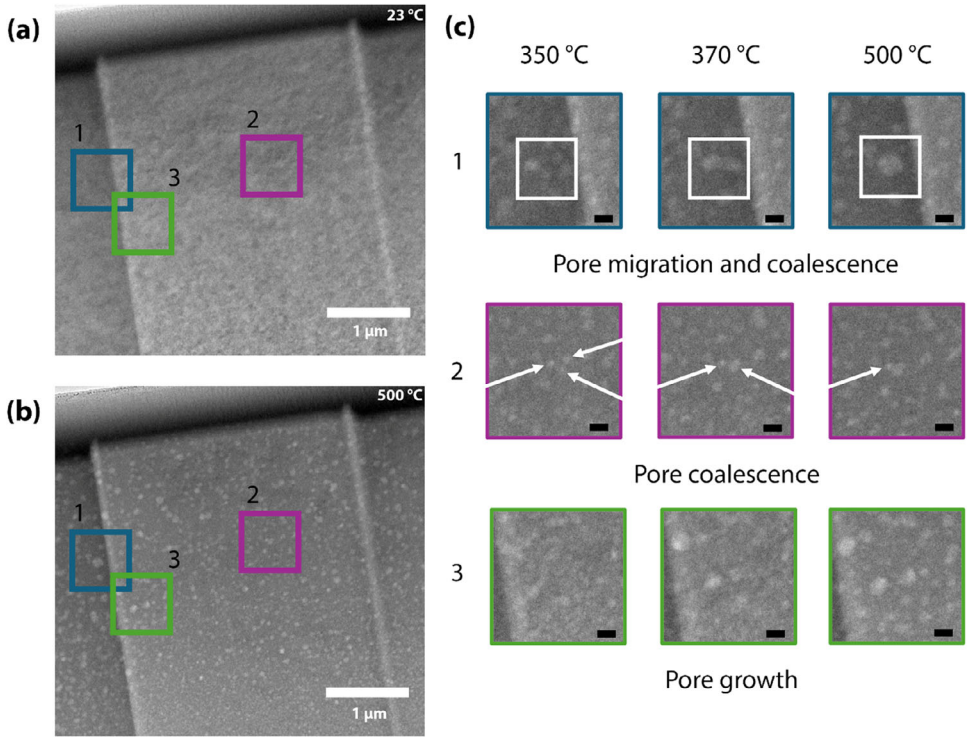

FIGURE 7 | TEM bright field images recorded while heating lamella. The lamella contains 3 steps of thickness 990, 750, 930 nm from left to right in (a) and (b) (see also Figure S14). (a) The lamella at room temperature, (b) the lamella at 500°C, and (c) magnified areas 1–3 (indicated by boxed regions in (a) and (b)) during heating at 350°C, 370°C, 500°C. These highlight pore movement, coalescence (arrows) and growth, with area 1 ultimately displaying a faceted pore (see box). Scale bars = 100 nm. These data are also shown in Movies S4 and S5.

medium without infiltration of the external fluid into the pores. This means that the pores are not compromised during dispersion in liquid media, milling, or compounding, making the system extremely robust. The sizes and shapes of the crystals can also be defined at the point of synthesis using well-established methods such as varying the supersaturation and temperature, and through the addition of crystal growth additives. While a full life-cycle assessment (LCA) comparing annealed porous calcite with TiO_2 or simple calcite nanoparticle pigment production would be needed to quantify the net sustainability benefit of our approach, the improved scattering efficiency of our developed material is expected to reduce the total material consumption.

It is interesting to compare the crystal structures generated using the three contrasting additives. The use of PS spheres as sacrificial templates yielded a uniform population of pores closely matching the size of the original spheres, while occlusion of polymer vesicles resulted in a wide range of pore sizes and shapes. Surprisingly, encapsulation of amino acids also gave extensive porosity, despite their significantly lower levels of occlusion. Investigation of the mechanism of pore formation highlighted the role of water co-entrapped within the crystal. Significant amounts of water are entrapped within the vesicles, which facilitates recrystallisation during annealing, and the development of irregular pore shapes. Water is also key to pore development in the calcite/ amino acid system, where co-occluded water molecules enable pore formation at temperatures well below the decomposition threshold of the amino acids.

After small pores have formed, the system can reduce its energy through growth of the pores, either via pore coalescence or an Ostwald ripening mechanism in which larger pores grow at the expense of smaller ones, reducing the entire surface area/ volume ratio of pores in the crystal. These processes are driven by ion migration, with surface diffusion at the pore/crystal boundaries occurring at lower temperatures than diffusion through the bulk of the crystal. Surface diffusion is expected to dominate once sufficient micropores have formed to exceed a percolation threshold [52]. The same energetic driving force also drives "healing" of the crystal structure after water and decomposition products are released, where the optical properties of the macroporous crystals demonstrate that the pores are air-filled.

Comparable mechanisms have also been observed during the annealing of sea urchin skeletal elements, where these biominerals behave as calcite single crystals and develop porosity on heating [54]. However, in contrast to the synthetic crystals generated here, they contain amorphous calcium carbonate (ACC) and proteins [54]. Small angle x-ray scattering (SAXS) showed that pores first formed around 170°C in sea urchin spines, where this was principally attributed to the release of water during ACC crystallisation. The pores increased in number and size as the temperature was increased to 450°C and the decomposition of organics dominated, and pore coarsening occurred via an Ostwald ripening mechanism. That our synthetic composite crystals also develop porosity demonstrates that occluded ACC is not a prerequisite to pore formation.

Most previous work synthesising porous calcium carbonate has delivered mesoporous particles. Mesoporosity often accompanies the formation of vaterite particles, where these are almost exclusively polycrystalline [64–67]. However, as a kinetic polymorph, they are also inherently unstable in solution and transform to the more stable calcite or aragonite polymorphs [65]. A number of alternative strategies such as transforming assemblies of ACC nanoparticles have also been explored [68, 69]. Considering macroporous particles, hollow $CaCO_3$ shells have been formed by the templating of gas bubbles [70], and precipitation in the presence of polymer/ surfactant mixtures [71–74]. However, while these fall in the required size regime to act as effective scatterers [75], they are often fragile and invariably permeable.

Finally, it is useful to consider our strategy in light of the methods used to synthesise macroporous ceramics [1, 4, 14, 76]. Many of these are also based on templating approaches [77], where direct foaming creates macroporous structures by introducing gas bubbles into a ceramic slurry, while replica methods typically coat a polymer foam with a ceramic slurry and subsequent annealing removes the polymer to generate a ceramic with a structure resembling the original foam [4]. Gel-casting is a related process where organic gelling agents are used to template the porous ceramic. The approach most closely related to the strategy developed here is sacrificial templating, in which pore-forming organic or polymeric substances such as starch or polymer beads are combined with ceramic powders, before annealing to eliminate the organics and generate porosity [78]. This offers a simple, adaptable means of controlling pore structure that is capable of generating both open and closed pores. These techniques differ in scalability and deliver products with varying porosity, pore structure, and mechanical strength. Notably, while most can be shaped into monoliths of the desired size and shape, as required for many applications, none can generate macroporous particles with well-defined sizes and shapes.

4 | Conclusions

This work demonstrates a straightforward strategy that can transform single crystals into unique macroporous single crystals with defined external sizes and shapes. Using calcium carbonate as a model system, PS spheres, vesicles, and amino acids were entrapped within calcite crystals using a simple one-pot method, and closed-cell macroporosity was created by annealing. The low cost and ease of scale-up makes the occlusion of amino acids particularly attractive, where pore formation can be attributed to water co-entrapped with the amino acids. We then demonstrate an application of these macroporous crystals as whitening agents. Materials such as $BaSO_4$, $CaCO_3$ and kaolinite offer environmentally-friendly alternatives to titania, but their lower refractive indices render them inferior in terms of opacity and brightness [37]. By introducing sub-micron macroporosity into calcite single crystals, which enables the multiple scattering of light, we create crystals whose optical properties remain invariant when dispersed in different carrier fluids, and the uniformity in size and shape optimises properties such as opacity and gloss. With the ability to control the porosity and the size and shape of the crystals, and to extend the strategy to alternative crystalline materials, many of which have already been shown to occlude additives [27, 31, 79–81], this approach offers a powerful new means of synthesising macroporous crystals.

Acknowledgements

We would like to acknowledge the support of the EPSRC and Imerys Minerals Limited for supporting an iCASE studentship (EP/N509681/1, NE/W503125/1) awarded to SEF. This work was supported by an EPSRC Programme Grant which funds the "Crystallization in the Real World" Consortium (No. EP/R018820/1, SEF, YYK, FCM, RDB). EPSRC grants EP/X040992/1, EP/V028855/1, EP/P00122X/1 and EP/M028143/1 supported provision of staffing and FIBSEM and TEM facilities in the LEMAS facility, University of Leeds. We acknowledge the ERC for funding the EXTREME grant, grant agreement number 101019499 (MJD and TK), and TK was also funded by an Oppenheimer Studentship (University of Cambridge). This work was also supported by the European Research Council (ERC-2014-STG H2020 639088), and the VALUED Program Grant EPSRC EP/W031019/1.

Funding

This work was funded by EPSRC: EP/N509681/1, NE/W503125/1, EP/R018820/1, EP/X040992/1, EP/V028855/1, EP/P00122X/1, EP/M028143/1 and EP/W031019/1 and European Research Council: EXTREME 101019499 and ERC-2014-STG H2020 639088.

Conflicts of Interest

The authors declare no conflicts of interest.

Data Availability Statement

For open access purposes, the authors have applied a CC-BY public copyright license to any Author Accepted Manuscript (AAM) version arising from this submission. The data associated with this paper are openly available from the Research Data Leeds Repository at https://doi.org/10.5518/1724 [82].

References

1. E. C. Hammel, O. L. R. Ighodaro, and O. I. Okoli, "Processing and Properties of Advanced Porous Ceramics: An Application Based Review," *Ceramics International* 40 (2014): 15351–15370, https://doi.org/10.1016/j.ceramint.2014.06.095.

2. R. Freund, S. Canossa, S. M. Cohen, et al., "25 Years of Reticular Chemistry," *Angewandte Chemie International Edition* 60 (2021): 23946–23974, https://doi.org/10.1002/anie.202101644.

3. G. R. Cai, P. Yan, L. L. Zhang, H. C. Zhou, and H. L. Jiang, "Metal–Organic Framework-Based Hierarchically Porous Materials: Synthesis and Applications," *Chemical Reviews* 121 (2021): 12278–12326, https://doi.org/10.1021/acs.chemrev.1c00243.

4. Siddharth and R. Siddhartha, "Advanced Applications and Processing Techniques for Porous Ceramics," in *Advanced Smart and Multifunctional Materials Volume 2: Advanced Processing, Polymers, Ceramics, and Related Functional Materials* (American Chemical Society, 2025), 1–41.

5. M. D. Oleksiak and J. D. Rimer, "Synthesis of Zeolites in the Absence of Organic Structure-Directing Agents: Factors Governing Crystal Selection and Polymorphism," *Reviews in Chemical Engineering* 30 (2014): 1–49, https://doi.org/10.1515/revce-2013-0020.

6. J. H. Yu and R. R. Xu, "Rational Approaches Toward the Design and Synthesis of Zeolitic Inorganic Open-Framework Materials," *Accounts of Chemical Research* 43 (2010): 1195–1204, https://doi.org/10.1021/ar900293m.

7. M. Y. Shao, N. T. Ramirez-Márquez, Z. D. Liu, and J. Garcia-Martinez, "Harnessing Kinetic Control in Zeolite Synthesis and Interconversion

to Enhance Catalytic Performance," *CCS Chemistry* 8 (2026): 1762–1779, https://doi.org/10.31635/ccschem.026.202507217.

8. Y. Zhai, Q. M. Wu, F. Y. Xiang, and F. S. Xiao, "Recent Syntheses of Novel Zeolites With Different Pore Sizes," *Dalton Transactions* 55 (2026): 1625–1636, https://doi.org/10.1039/D5DT02510A.

9. X. F. Ma, J. Q. Zhao, and H. L. Zheng, "Rational Crystal Engineering of Metal–Organic Frameworks for Tailored Structure and Function," *Crystengcomm* 28 (2026): 329–343, https://doi.org/10.1039/D5CE00974J.

10. Z. B. Wang, H. Y. Chu, M. Chang, and C. C. Wang, "Tailoring Metal–Organic Frameworks: From morphological control to superstructure assembly," *Coordination Chemistry Reviews* 554 (2026): 217606, https://doi.org/10.1016/j.ccr.2026.217606.

11. M. Y. Zhang, H. J. Zhou, S. Y. Gu, et al., "Tailoring Nano-Metal-Organic Frameworks and Their Derivatives: From Morphology Engineering to Structural and Functional Optimization," *Advanced Materials* 38 (2026): 16446.

12. S. H. Wu, C. Y. Mou, and H. P. Lin, "Synthesis of Mesoporous Silica Nanoparticles," *Chemical Society Reviews* 42 (2013): 3862–3875, https://doi.org/10.1039/c3cs35405a.

13. R. Narayan, U. Y. Nayak, A. M. Raichur, and S. Garg, "Mesoporous Silica Nanoparticles: A Comprehensive Review on Synthesis and Recent Advances," *Pharmaceutics* 10 (2018): 118, https://doi.org/10.3390/pharmaceutics10030118.

14. A. R. Studart, U. T. Gonzenbach, E. Tervoort, and L. J. Gauckler, "Processing Routes to Macroporous Ceramics: A Review," *Journal of the American Ceramic Society* 89 (2006): 1771–1789, https://doi.org/10.1111/j.1551-2916.2006.01044.x.

15. Y. Chen, N. N. Wang, O. Ola, Y. D. Xia, and Y. Q. Zhu, "Porous Ceramics: Light in Weight but Heavy in Energy and Environment Technologies," *Materials Science and Engineering Reports* 143 (2021): 100589.

16. Z. F. Deng, Z. A. Jia, and L. Li, "Biomineralized Materials as Model Systems for Structural Composites: Intracrystalline Structural Features and Their Strengthening and Toughening Mechanisms," *Advanced Science* 9 (2022): 2103524.

17. Y. Xu, J. M. Galloway, L. J. Hasselt, and F. C. Meldrum, "The Role of Confinement in Biomineralization," *Chemical Reviews* 125 (2025): 12128–12197, https://doi.org/10.1021/acs.chemrev.5c00659.

18. U. G. K. Wegst, H. Bai, E. Saiz, A. P. Tomsia, and R. O. Ritchie, "Bioinspired Structural Materials," *Nature Materials* 14 (2015): 23–36, https://doi.org/10.1038/nmat4089.

19. J. Y. Sun and B. Bhushan, "Hierarchical Structure and Mechanical Properties of Nacre: A Review," *RSC Advances* 2 (2012): 7617–7632, https://doi.org/10.1039/c2ra20218b.

20. J. Aizenberg, J. Hanson, T. F. Koetzle, S. Weiner, and L. Addadi, "Control of Macromolecule Distribution Within Synthetic and Biogenic Single Calcite Crystals," *Journal of the American Chemical Society* 119 (1997): 881–886, https://doi.org/10.1021/ja9628821.

21. H. Y. Li, H. L. Xin, M. E. Kunitake, E. C. Keene, D. A. Muller, and L. A. Estroff, "Calcite Prisms From Mollusk Shells (Atrina Rigida): Swiss-Cheese-Like Organic–Inorganic Single-Crystal Composites," *Advanced Functional Materials* 21 (2011): 2028–2034, https://doi.org/10.1002/adfm.201002709.

22. J. Seto, Y. R. Ma, S. A. Davis, et al., "Structure-Property Relationships of a Biological Mesocrystal in the Adult Sea Urchin Spine," *Proceedings of the National Academy of Sciences* 109 (2012): 3699–3704, https://doi.org/10.1073/pnas.1109243109.

23. Y.-Y. Kim, J. D. Carloni, B. Demarchi, et al., "Tuning Hardness in Calcite by Incorporation of Amino Acids," *Nature Materials* 15 (2016): 903–910, https://doi.org/10.1038/nmat4631.

24. D. C. Green, J. Ihli, Y. Y. Kim, et al., "Rapid Screening of Calcium Carbonate Precipitation in the Presence of Amino Acids: Kinetics, Structure, and Composition," *Crystal Growth & Design* 16 (2016): 5174–5183, https://doi.org/10.1021/acs.cgd.6b00741.

25. G. Magnabosco, M. Di Giosia, I. Polishchuk, et al., "Calcite Single Crystals as Hosts for Atomic-Scale Entrapment and Slow Release of Drugs," *Advanced Healthcare Materials* 4 (2015): 1510–1516, https://doi.org/10.1002/adhm.201500170.

26. S. Borukhin, L. Bloch, T. Radlauer, A. H. Hill, A. N. Fitch, and B. Pokroy, "Screening the Incorporation of Amino Acids Into an Inorganic Crystalline Host: The Case of Calcite," *Advanced Functional Materials* 22 (2012): 4216–4224, https://doi.org/10.1002/adfm.201201079.

27. Y. Y. Kim, R. Darkins, A. Broad, et al., "Hydroxyl-Rich Macromolecules Enable the Bio-Inspired Synthesis of Single Crystal Nanocomposites," *Nature Communications* 10 (2019): 5682, https://doi.org/10.1038/s41467-019-13422-9.

28. Y. Y. Kim, K. Ganesan, P. C. Yang, et al., "An Artificial Biomineral Formed by Incorporation of Copolymer Micelles in Calcite Crystals," *Nature Materials* 10 (2011): 890–896, https://doi.org/10.1038/nmat3103.

29. O. Nahi, A. N. Kulak, T. Kress, et al., "Incorporation of Nanogels Within Calcite Single Crystals for the Storage, Protection and Controlled Release of Active Compounds," *Chemical Science* 12 (2021): 9839–9850, https://doi.org/10.1039/D1SC02991F.

30. Y. Y. Kim, L. A. Fielding, A. N. Kulak, et al., "Influence of the Structure of Block Copolymer Nanoparticles on the Growth of Calcium Carbonate," *Chemistry of Materials* 30 (2018): 7091–7099, https://doi.org/10.1021/acs.chemmater.8b02912.

31. A. N. Kulak, R. Grimes, Y. Y. Kim, et al., "Polymer-Directed Assembly of Single Crystal Zinc Oxide/Magnetite Nanocomposites Under Atmospheric and Hydrothermal Conditions," *Chemistry of Materials* 28 (2016): 7528–7536, https://doi.org/10.1021/acs.chemmater.6b03563.

32. M. Calvaresi, G. Falini, L. Pasquini, et al., "Morphological and Mechanical Characterization of Composite Calcite/SWCNT–COOH Single Crystals," *Nanoscale* 5 (2013): 6944–6949, https://doi.org/10.1039/c3nr01568h.

33. A. N. Kulak, M. Semsarilar, Y. Y. Kim, et al., "One-pot Synthesis of an Inorganic Heterostructure: Uniform Occlusion of Magnetite Nanoparticles Within Calcite Single Crystals," *Chemical Science* 5 (2014): 738–743, https://doi.org/10.1039/C3SC52615A.

34. Y.-Y. Kim, L. Ribeiro, F. Maillot, O. Ward, S. J. Eichhorn, and F. C. Meldrum, "Bio-Inspired Synthesis and Mechanical Properties of Calcite–Polymer Particle Composites," *Advanced Materials* 22 (2010): 2082–2086.

35. B. Marzec, J. Walker, Y. Jhons, F. C. Meldrum, M. Shaver, and F. Nudelman, "Micron-Sized Biogenic and Synthetic Hollow Mineral Spheres Occlude Additives Within Single Crystals," *Faraday Discussions* 235 (2022): 536–550.

36. O. Nahi, A. Broad, A. N. Kulak, et al., "Positively Charged Additives Facilitate Incorporation in Inorganic Single Crystals," *Chemistry of Materials* 34 (2022): 4910–4923, https://doi.org/10.1021/acs.chemmater.2c00097.

37. J. Radtke, R. Wiedey, and P. Kleinebudde, "Alternatives to Titanium Dioxide in Tablet Coating," *Pharmaceutical Development and Technology* 26 (2021): 989–999, https://doi.org/10.1080/10837450.2021.1968900.

38. L. Schertel, I. Wimmer, P. Besirske, et al., "Tunable High-Index Photonic Glasses," *Physical Review Materials* 3 (2019): 015203, https://doi.org/10.1103/PhysRevMaterials.3.015203.

39. F. Wu, Z. Zhou, and A. L. Hicks, "Life Cycle Impact of Titanium Dioxide Nanoparticle Synthesis Through Physical, Chemical, and Biological Routes," *Environmental Science & Technology* 53 (2019): 4078–4087, https://doi.org/10.1021/acs.est.8b06800.

40. Z. Luo, Z. Q. Li, Z. Xie, et al., "Rethinking Nano-TiO_2 Safety: Overview of Toxic Effects in Humans and Aquatic Animals," *Small* 16 (2020): 2002019, https://doi.org/10.1002/smll.202002019.

41. H. M. Braakhuis, I. Gosens, M. B. Heringa, et al., "Mechanism of Action of TiO_2: Recommendations to Reduce Uncertainties Related to

Carcinogenic Potential," *Annual Review of Pharmacology and Toxicology* 61 (2021): 203–223, https://doi.org/10.1146/annurev-pharmtox-101419-100049.

42. Y. Wu, L. Chen, F. Chen, H. Zou, and Z. Wang, "A Key Moment for TiO_2: Prenatal Exposure to TiO_2 Nanoparticles May Inhibit the Development of Offspring," *Ecotoxicology and Environmental Safety* 202 (2020): 110911, https://doi.org/10.1016/j.ecoenv.2020.110911.

43. G. I. Dar, M. Saeed, and A. Wu, Toxicity of TiO_2 Nanoparticles, in *TiO_2 Nanoparticles*, (Eds.: A. Wu and W. Ren) (Wiley, 2020), 67–103, https://doi.org/10.1002/9783527825431.ch2.

44. European Chemicals Agency, (ECHA), Committee for Risk Assessment (RAC), Opinion Proposing Harmonised Classification and Labelling at EU Level of Titanium Dioxide, CLH-O-0000001412-86-163/F, 14 September, (2017).

45. J. Ihli, P. Bots, A. Kulak, L. G. Benning, and F. C. Meldrum, "Elucidating Mechanisms of Diffusion-Based Calcium Carbonate Synthesis Leads to Controlled Mesocrystal Formation," *Advanced Functional Materials* 23 (2013): 1965–1973, https://doi.org/10.1002/adfm.201201742.

46. G. Jacucci, B. W. Longbottom, C. C. Parkins, S. A. F. Bon, and S. Vignolini, "Anisotropic Silica Colloids for Light Scattering," *Journal of Materials Chemistry C* 9 (2021): 2695–2700, https://doi.org/10.1039/D1TC00072A.

47. M. S. Toivonen, O. D. Onelli, G. Jacucci, et al., "Anomalous-Diffusion-Assisted Brightness in White Cellulose Nanofibril Membranes," *Advanced Materials* 30 (2018): 1704050, https://doi.org/10.1002/adma.201704050.

48. J. Syurik, G. Jacucci, O. D. Onelli, H. Hölscher, and S. Vignolini, "Bio-Inspired Highly Scattering Networks via Polymer Phase Separation," *Advanced Functional Materials* 28 (2018): 1706901, https://doi.org/10.1002/adfm.201706901.

49. H. Yang, G. Jacucci, L. Schertel, and S. Vignolini, "Cellulose-Based Scattering Enhancers for Light Management Applications," *ACS Nano* 16 (2022): 7373–7379, https://doi.org/10.1021/acsnano.1c09198.

50. G. Jacucci, J. Bertolotti, and S. Vignolini, "Role of Anisotropy and Refractive Index in Scattering and Whiteness Optimization," *Advanced Optical Materials* 7 (2019): 1900980, https://doi.org/10.1002/adom.201900980.

51. S. Mijowska, I. Polishchuk, A. Lang, et al., "High Amino Acid Lattice Loading at Nonambient Conditions Causes Changes in Structure and Expansion Coefficient of Calcite," *Chemistry of Materials* 32 (2020): 4205–4212, https://doi.org/10.1021/acs.chemmater.0c00428.

52. M. Albéric, E. Zolotoyabko, O. Spaeker, et al., "Heat-Mediated Micro- and Nano-Pore Evolution in Sea Urchin Biominerals," *Crystal Growth & Design* 22 (2022): 3727–3739.

53. K. Mann, A. J. Poustka, and M. Mann, "The Sea Urchin (Strongylocentrotus purpuratus) Test and Spine Proteomes," *Proteome Science* 6 (2008): 22, https://doi.org/10.1186/1477-5956-6-22.

54. M. Albéric, E. N. Caspi, M. Bennet, et al., "Interplay Between Calcite, Amorphous Calcium Carbonate, and Intracrystalline Organics in Sea Urchin Skeletal Elements," *Crystal Growth & Design* 18 (2018): 2189–2201.

55. I. M. Weiss, C. Muth, R. Drumm, and H. O. K. Kirchner, "Thermal Decomposition of the Amino Acids Glycine, Cysteine, Aspartic Acid, Asparagine, Glutamic Acid, Glutamine, Arginine and Histidine," *BMC Biophysics* 11 (2018): 2, https://doi.org/10.1186/s13628-018-0042-4.

56. O. A. Jimoh, K. S. Ariffin, H. Bin Hussin, and A. E. Temitope, "Synthesis of Precipitated Calcium Carbonate: A Review," *Carbonates and Evaporites* 33 (2018): 331–346, https://doi.org/10.1007/s13146-017-0341-x.

57. S. Zide, H. Ho, L. Petrik, T. Ojumu, and A. Iizuka, "Assessment of the Potential Industrial Applications of Calcium Carbonate Derived From Mineral Carbonation of Alkaline Waste Material," *International Journal of Environmental Science and Technology* 23 (2025): 82.

58. N. Erdogan and H. A. Eken, "Precipitated Calcium Carbonate Production, Synthesis and Properties," *Physicochem Probl Miner Process* 53 (2017): 57–68.

59. F. Karakas, B. V. Hassas, and M. S. Çelik, "Effect of Precipitated Calcium Carbonate Additions on Waterborne Paints at Different Pigment Volume Concentrations," *Progress in Organic Coatings* 83 (2015): 64–70, https://doi.org/10.1016/j.porgcoat.2015.02.003.

60. W. L. Bragg, "The Refractive Indices of Calcite and Aragonite," *Proceedings of the Royal Society of London Series A, Containing Papers of a Mathematical and Physical Character* 105 (1924): 370–386, https://doi.org/10.1098/rspa.1924.0026.

61. H. Tang, H. Berger, P. E. Schmid, and F. Levy, "Optical Properties of Anatase(TiO_2)," *Solid State Communications* 92 (1994): 267–271.

62. J. Rams, A. Tejeda, and J. M. Cabrera, "Refractive Indices of Rutile as a Function of Temperature and Wavelength," *Journal of Applied Physics* 82 (1997): 994–997, https://doi.org/10.1063/1.365938.

63. G. Jacucci, L. Schertel, Y. Zhang, H. Yang, and S. Vignolini, "Light Management With Natural Materials: From Whiteness to Transparency," *Advanced Materials* 33 (2021): 2001215, https://doi.org/10.1002/adma.202001215.

64. J. G. Yu, J. C. Yu, L. Z. Zhang, X. C. Wang, and L. Wu, "Facile Fabrication and Characterization of Hierarchically Porous Calcium Carbonate Microspheres," *Chemical Communications* 21 (2004): 2414–2415, https://doi.org/10.1039/b406839d(2004.

65. S. Y. Kim, M. K. Kang, A. R. Min, et al., "Engineering Porous Vaterite $CaCO_3$ Nanostructures via Alcohol–Surfactant Coordination in Co-Precipitation: A facile Route to Tunable Drug-Carrier Platforms," *Colloids and Surfaces B: Biointerfaces* 263 (2026): 115592, https://doi.org/10.1016/j.colsurfb.2026.115592.

66. R. Febrida, A. Cahyanto, E. Herda, et al., "Synthesis and Characterization of Porous $CaCO_3$ Vaterite Particles by Simple Solution Method," *Materials* 14 (2021): 4425, https://doi.org/10.3390/ma14164425.

67. N. Zhang, B. H. Zhao, P. Yang, and H. F. Zhang, "Systematic Study of Preparing Porous $CaCO_3$ Vaterite Particles for Controlled Drug Release," *Nanomaterials* 15 (2025): 1227.

68. D. Gebauer, X. M. Liu, B. Aziz, N. Hedin, and Z. Zhao, "Porous Tablets of Crystalline Calcium Carbonate via Sintering of Amorphous Nanoparticles," *Crystengcomm* 15 (2013): 1257–1263, https://doi.org/10.1039/c2ce26604k.

69. R. Sun, T. Willhammar, E. S. Grape, M. Stromme, and O. Cheung, "Mesoscale Transformation of Amorphous Calcium Carbonate to Porous Vaterite Microparticles With Morphology Control," *Crystal Growth & Design* 19 (2019): 5075–5087, https://doi.org/10.1021/acs.cgd.9b00438.

70. G. Hadiko, Y. S. Han, M. Fuji, and M. Takahashi, "Synthesis of Hollow Calcium Carbonate Particles by the Bubble Templating Method," *Materials Letters* 59 (2005): 2519–2522, https://doi.org/10.1016/j.matlet.2005.03.036.

71. L. N. Zhao and J. K. Wang, "Biomimetic Synthesis of Hollow Microspheres of Calcium Carbonate Crystals in the Presence of Polymer and Surfactant," *Colloids and Surfaces A: Physicochemical and Engineering Aspects* 393 (2012): 139–143, https://doi.org/10.1016/j.colsurfa.2011.11.012.

72. T. W. Zheng, H. H. Yi, S. Y. Zhang, and C. G. Wang, "Preparation and Formation Mechanism of Calcium Carbonate Hollow Microspheres," *Journal of Crystal Growth* 549 (2020): 125870, https://doi.org/10.1016/j.jcrysgro.2020.125870.

73. J. G. Yu, X. F. Zhao, B. Cheng, and Q. J. Zhang, "Controlled Synthesis of Calcium Carbonate in a Mixed Aqueous Solution of PSMA and CTAB," *Journal of Solid State Chemistry* 178 (2005): 861–867, https://doi.org/10.1016/j.jssc.2005.01.002.

74. T. W. Zheng, X. Zhang, and H. H. Yi, "Spherical Vaterite Microspheres of Calcium Carbonate Synthesized With Poly (acrylic acid) and Sodium Dodecyl Benzene Sulfonate," *Journal of Crystal Growth* 528 (2019): 125275, https://doi.org/10.1016/j.jcrysgro.2019.125275.

75. N. S. Sukhinina, V. M. Masalov, J. Yu, et al., "A Promising White Pigment Based on Hollow Spherical Silica Particles," *Colloids and Surfaces A: Physicochemical and Engineering Aspects* 726 (2025): 137909, https://doi.org/10.1016/j.colsurfa.2025.137909.

76. T. Ohji and M. Fukushima, "Macro-Porous Ceramics: Processing and Properties," *International Materials Reviews* 57 (2012): 115–131, https://doi.org/10.1179/1743280411Y.0000000006.

77. A. Feinle, M. S. Elsaesser, and N. Hüsing, "Sol–gel Synthesis of Monolithic Materials With Hierarchical Porosity," *Chemical Society Reviews* 45 (2016): 3377–3399, https://doi.org/10.1039/C5CS00710K.

78. M. L. Jalaluddin, U. A. Azlan, M. W. Abd Rashid, N. Tamin, and M. N. Masri, "A Review of Pore-Forming Agents on the Structures, Porosities, and Mechanical Properties of Porous Ceramics," *AIMS Mater Sci* 11 (2024): 634–665.

79. B. Kahr and R. W. Gurney, "Dyeing Crystals," *Chemical Reviews* 101 (2001): 893–952, https://doi.org/10.1021/cr980088n.

80. Y. Y. Kim, A. S. Schenk, D. Walsh, A. N. Kulak, O. Cespedes, and F. C. Meldrum, "Bio-Inspired Formation of Functional Calcite/Metal Oxide Nanoparticle Composites," *Nanoscale* 6 (2014): 852–859, https://doi.org/10.1039/C3NR05081E.

81. Y. Ning, L. A. Fielding, J. Nutter, A. N. Kulak, F. C. Meldrum, and S. P. Armes, "Spatially Controlled Occlusion of Polymer-Stabilized Gold Nanoparticles Within ZnO," *Angewandte Chemie International Edition* 58 (2019): 4302–4307, https://doi.org/10.1002/anie.201814492.

82. S. E. Foster, G. Jacucci, O. Nahi, et al., Dataset for "Bio-Inspired Synthesis of Macroporous Single Crystal Particles as Scattering Agents", (2025), https://doi.org/10.5518/1724.

Supporting Information

Additional supporting information can be found online in the Supporting Information section.

Supporting File 1: adfm76652-sup-0001-SuppMat.docx.

Supporting File 2: adfm76652-sup-0002-MovieS1.mp4.

Supporting File 3: adfm76652-sup-0003-MovieS2.mp4.

Supporting File 4: adfm76652-sup-0004-MovieS3.mp4.

Supporting File 5: adfm76652-sup-0005-MovieS4.mp4.

Supporting File 6: adfm76652-sup-0006-MovieS5.mp4.